

Antisite Defect Si_C as a Source of the D_I Center in 4H-SiC

Hai-Shan Zhang, Jian Gong,* and Lin Shi*

D_I center, as a widely existed defect in 4H-SiC, has attracted much attention in recent years, while the origin of it is still unclear. Herein, by comparing first-principles calculated potential point defects-related zero-phonon lines (ZPLs) and nonradiative capture cross-sections with the D_I center-related values in the experiment, it is proposed that the transition from the bound exciton states about 57 meV below the CBM to the “+1/+2” level of antisite defect Si_C is responsible for the D_I center in 4H-SiC. This work describes the temperature and transition energy level dependence of the hole capture cross-section of antisite defect $\text{Si}_\text{C}^\text{h}$ in 4H-SiC, which provides an idea for the optimal design of point defects in semiconductor materials.

1. Introduction

Silicon carbide semiconductors (SiC) have become an outstanding wide bandgap semiconductor for transducers, high electron mobility transistors, and other applications due to their excellent thermal, mechanical, and physical properties.^[1–3] A variety of point defects may present in as-grown or irradiated SiC samples.^[4–7] On the downside, the efficiency of optoelectronic devices is reduced by deep-level centers capturing free carriers.^[7] On the upside, it has been proved that some defect centers in 4H-SiC semiconductors can be used as single-photon sources.^[6] Therefore, the efficient application of SiC materials requires a clear understanding of the nature of the point defects, especially the identification of the defect types.

As one of the most important defects in 4H-SiC, D_I center has been followed with wide interest and studied.^[7–15] The D_I defect center can be observed in low-temperature luminescence spectra of as-grown and high-energy-particle (ions, neutrons, or electrons) bombardment 4H-SiC samples followed by high-temperature annealing. At low temperature ($T < 5$ K), the D_I

spectrum in 4H-SiC main consists of one ZPL L_1 (2.902 eV). As the temperature is raised ($T = 40$ K), two higher energy ZPLs, M_1 (2.910 eV) and H_1 (2.913 eV), appear while the L_1 intensity rapidly decreases.^[15] Investigation of the photoelectric properties revealed that the D_I center results from the transition between a series of exciton states and a hole trap state. The activation energies of the exciton states are ≈ 57 meV,^[15] and the associated hole trap named HS1 center at 0.35 eV above the valence band maximum (VBM).^[10] Deep-level transient spectroscopy (DLTS)


confirms that the hole capture cross-section of D_I center was $2 \times 10^{-14} \text{ cm}^2$.^[7] Many works have focused on understanding the origins of the D_I defect. Maximenko et al. proposed that the change in intensity of the D_I defect correlates with the change of the electron paramagnetic resonance (EPR) signal of divacancies ($\text{V}_\text{C}-\text{V}_\text{Si}$) at a temperature above 1900 °C.^[16] However, by first-principles calculations, Gu and Magnusson et al. proposed that the transition levels of the inequivalent $\text{V}_\text{C}-\text{V}_\text{Si}$ defects range from 1.1 to 1.75 eV, which are far from the experimental value of D_I center (0.35 eV).^[17,18] Zhang et al. proposed that in silicon-rich growth samples, D_I defect concentration decreased with the increase of the C/Si ratio.^[7] Many works attributed the D_I center to the antisite pair ($\text{Si}_\text{C}-\text{C}_\text{Si}$). However, Posselt et al. reported that the $\text{Si}_\text{C}-\text{C}_\text{Si}$ had high formation energy and was unstable at 2000 K, which should not be related to the stable D_I center above 2000 K.^[19] Eberlein et al. proposed that isolated silicon antisite (Si_C) might be responsible for the D_I center by calculating the defects-related local phonon mode and defect stability.^[14] However, they did not provide other direct evidence and explanation. Although this topic has been widely discussed, the specific origin of the D_I center is still an open question. Nowadays, state-of-the-art first-principles calculations can provide relatively accurate defect energy level positions, defect-related luminescence, as well as carrier capture cross-sections of deep defect centers. Therefore, we were inspired to identify the origin of the D_I centers by combining first-principles calculations with the DLTS and photoluminescence experimental results of 4H-SiC.

In this work, we systematically study the formation energy, optical transitions, and carrier capture cross-section of antisite defect in 4H-SiC-based first-principles calculations. We show that the transition level of “+1/+2” of $\text{Si}_\text{C}^\text{h}$ is located at $E_\text{VBM} + 0.31$ eV, and the transition from the bound exciton to the “+1/+2” level of $\text{Si}_\text{C}^\text{h}$ defect can cause a ZPL emission at 2.883 eV, which is highly consistent with the emission peak of D_I center in the experiment. Furthermore, by comparing the calculated and experimental hole capture cross-section, we

H.-S. Zhang, J. Gong
School of Physical Science and Technology
Inner Mongolia University
Hohhot 010021, P. R. China
E-mail: ndgong@imu.edu.cn

J. Gong
College of Physics and Electronic Information
Inner Mongolia Normal University
Hohhot 010021, P. R. China

L. Shi
School of Materials Science and Engineering
Yancheng Institute of Technology
Yancheng 224051, P. R. China
E-mail: lshi2007@sinano.ac.cn

 The ORCID identification number(s) for the author(s) of this article can be found under <https://doi.org/10.1002/pssr.202200239>.

DOI: 10.1002/pssr.202200239

conclude that antisite defect Si_C is responsible for the D_1 center in 4H-SiC.

2. Calculation Details

Our first-principles calculations were performed on the basis of the density functional theory (DFT) method, as implemented in the PWmat software.^[20,21] The exchange-correlation potential was calculated by using the projector augmented wave (PAW) potentials with generalized gradient approximation (GGA) in the Perdew–Burke–Ernzerhof (PBE) format.^[22,23] The norm-conserving pseudopotentials of the SG15 version are used for Si and C.^[24] A 200-atom ($5 \times 5 \times 1$) supercell is used for the calculations of defects. The defective atomic structures were optimized with the mesh of a $1 \times 1 \times 1$ k -point grid using the screened functional of Heyd–Scuseria–Ernzerhof (HSE),^[25,26] and the mixing parameter (α) of HSE was set to 0.25. A kinetic energy cutoff of 60 Ry for the plane-wave basis set was used in all calculations, and the force criteria were $0.03 \text{ eV } \text{\AA}^{-1}$. The relaxed lattice parameters of bulk 4H-SiC, $a = 3.08 \text{ \AA}$, $c = 10.04 \text{ \AA}$, are in good agreement with the experimental results ($a = 3.08 \text{ \AA}$, $c = 10.08 \text{ \AA}$).^[27] The calculated bandgap of 4H-SiC is 3.25 eV, in good agreement with the experimental bandgap of 3.26 eV.^[3]

3. Result and Discussion

3.1. Defect Formation Energy

The 4H-SiC has two inequivalent lattice sites, cubic (k) and hexagonal (h), for C and Si. For the isolated antisite defects C_Si and Si_C , each defect has two inequivalent configurations, which can be represented as $(\text{C}_\text{Si}^h, \text{C}_\text{Si}^k)$ and $(\text{Si}_\text{C}^h, \text{Si}_\text{C}^k)$, respectively. The nearest Si_C defect and C_Si defect can combine together to form an antisite pair. In 4H-SiC, there are four inequivalent configurations, which are $\text{C}_\text{Si}^h\text{-Si}_\text{C}^h$, $\text{C}_\text{Si}^h\text{-Si}_\text{C}^k$, $\text{C}_\text{Si}^k\text{-Si}_\text{C}^h$, and $\text{C}_\text{Si}^k\text{-Si}_\text{C}^k$, respectively. As shown in Figure 1, we presented all the defects mentioned earlier in a supercell.

In this work, we first calculated the formation energies $\Delta H(a, q)$ of antisite and antisite pair defects according to the following formula^[28]

$$\Delta H(a, q) = E(a, q) - E(\text{host}) + \sum_i n_i (E_i + \mu_i) + q[E_{\text{VBM}}(\text{host}) + E_F + \Delta V] \quad (1)$$

$E(a, q)$ is the total energy of a supercell with a defect a in a charge state q , and $E(\text{host})$ is the total energy of the supercell without a defect. n_i is the number of elements C or Si removed from or added into the supercell, E_i is the total energy of C or Si at its elemental material, and μ_i is the chemical potential of atom i in the environment relative to elemental material. In this work, two limiting chemical potential conditions were considered, i.e., C-rich and Si-rich. Meanwhile, to ensure the successful formation of SiC, the chemical potentials μ_Si and μ_C need to meet the equation $\mu_\text{Si} + \mu_\text{C} = \Delta H(\text{SiC})$. $E_{\text{VBM}}(\text{host})$ is the energy of VBM, and E_F is the energy of the Fermi level with respect to VBM. ΔV is the energy difference between the core levels of atoms furthest

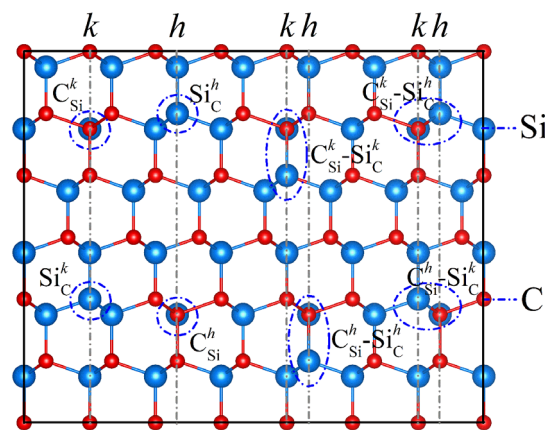


Figure 1. The atom structures of defects C_Si^h , C_Si^k , Si_C^h , Si_C^k , $\text{C}_\text{Si}^h\text{-Si}_\text{C}^h$, $\text{C}_\text{Si}^h\text{-Si}_\text{C}^k$, $\text{C}_\text{Si}^k\text{-Si}_\text{C}^h$, and $\text{C}_\text{Si}^k\text{-Si}_\text{C}^k$ in a 4H-SiC semiconductor. Si and C atoms have two inequivalent lattice sites, cubic (k) and hexagonal (h), respectively. Blue balls indicate the Si atoms, and red balls indicate the C atoms.

away from the defect center in defect cells to that of the perfect cells.

The calculated formation energies versus Fermi level for the aforementioned defects are shown in Figure 2. We have plotted only the lowest energy charge state at the Fermi level for each defect. Thus, the slope of the line segment corresponds to different charge states and the inflection point to thermodynamic charge state transition levels. The formation energy of the C_Si defect is lower than that of the Si_C defect under Si-poor chemical potential, while the opposite situation will occur under the Si-rich growth environment. The calculated transition energy levels of the aforementioned defects are shown in Table 1. The Si_C defect will generate deep energy levels in the bandgap, and the transition energy levels of two nonequivalent antisite defects (Si_C^h and Si_C^k) are similar. While the C_Si defect does not produce a deep energy level in the bandgap, which is consistent with the

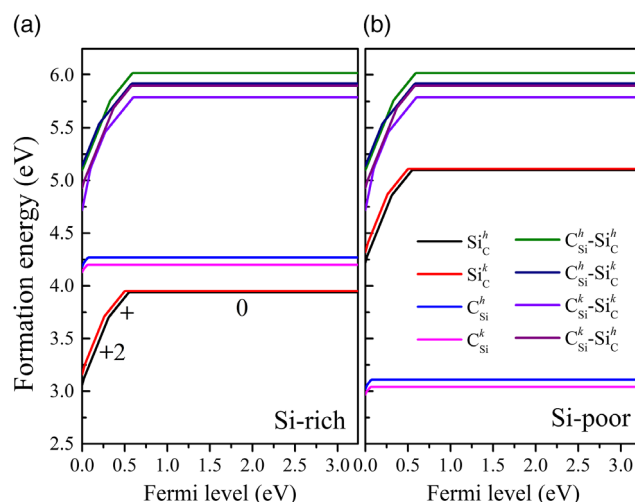


Figure 2. The defects formation energies of isolated antisite defects and first-neighbor antisite pairs as a function of Fermi level at different charge states in a) Si-rich and b) Si-poor growth conditions.

Table 1. Calculated transition levels of antisite and antisite pair defects. (the unit is eV).

	Si_C^h	Si_C^k	C_{Si}^h	C_{Si}^k	$\text{C}_{\text{Si}}^h\text{--Si}_\text{C}^h$	$\text{C}_{\text{Si}}^h\text{--Si}_\text{C}^k$	$\text{C}_{\text{Si}}^k\text{--Si}_\text{C}^h$	$\text{C}_{\text{Si}}^k\text{--Si}_\text{C}^k$
0/+1	0.55	0.51	0.08	0.07	0.60	0.59	0.61	0.59
+1/+2	0.31	0.27	–	–	0.34	0.21	0.27	0.38

conclusion of Ref. [29]. The four nonequivalent first-neighbor antisite defect pairs have similar transition energy levels, and their positions of “0/+1” and “+1/+2” energy levels in the bandgap are very close to those of Si_C defect, indicating that they have similar electronic structures to those of Si_C defect. However, the formation energies of antisite pairs are much higher than that of Si_C , indicating that the concentration of first-neighbor antisite pairs is much lower than that of the isolated defect. For isolated defect Si_C^h , the transition energy “0/+1” is located in $E_{\text{VBM}} + 0.55$ eV, and “+1/+2” is located in $E_{\text{VBM}} + 0.31$ eV, which is very close to the characteristic energy levels of D_I center in the experiment. In the minority carrier transient spectroscopy containing the D_I center (named HS1 center in their article), a hole capture center at $E_{\text{VBM}} + 0.61$ eV is also observed, which the authors tend to attribute to a boron-related deep center.^[7] Because the energy levels of $E_{\text{VBM}} + 0.55$ and $E_{\text{VBM}} + 0.61$ eV are relatively similar, we believe that the deep energy level at $E_{\text{VBM}} + 0.61$ eV accompanying with D_I center in their work may be related to the transition “0/+1” of defect Si_C . The transition level “+1/+2” of defect Si_C^k is located in $E_{\text{VBM}} + 0.27$ eV, which is 0.04 eV smaller than that of the defect Si_C^h . The two inequivalent Si_C defects are corresponding to the two sharp lines (L_1 and L_2) of D_I spectrum in the experiment.^[8] Since the antisite defects Si_C^h and Si_C^k have similar formation energies and transition energy levels, we only consider Si_C^h defect-related properties in this work.

3.2. Optical Transition of Si_C^h Defect

Figure 3a shows a series of Si_C^h defect-related transition processes. In n-type or semi-insulated 4H-SiC, the Si_C^h defect will present a fully occupied neutral charge state. Under excitation, the neutral defect can excite an electron to the conduction band or capture a hole from the valence band to change to a “+1” charge state. Then, a semi-occupied “+1” charge state defect can also change to a “+2” charge state by either exciting an electron to the conduction band or capturing a hole from the valence band. In the p-type 4H-SiC sample, the Si_C^h defect will present a “+2” charge state. When an electron in the high-energy state falls back to the “+2” charge state defect center, the defect will return to the “+1” charge state. As shown in Figure 3b, the ZPLs L_1 , M_1 , and H_1 of the D_I spectrum are due to the transition from the bound exciton about 57 meV below the CBM to the deep impurity level. Note, the exciton binding energy used here is cited from experimental work.^[15] Experimentally, at low temperature (4 K), only the L_1 line can be observed. As the temperature increase to about 40 K, the M_1 and H_1 lines appear while the L_1 intensity rapidly decreases. This may be because, prior to recombination, the excitons created in the M_1 and H_1 states relax

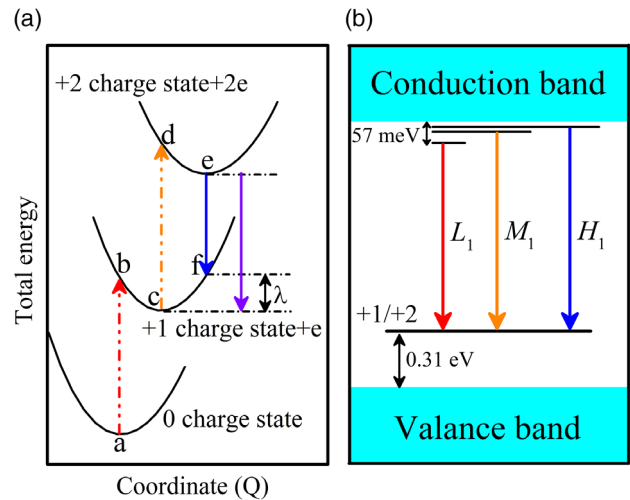


Figure 3. a) The configuration coordinate diagram shows a series of defect-related carrier transition processes. a→b and c→d are excited processes from “0” to “+1” and from “+1” to “+2” charge states, respectively. e→f is a de-excited process from “+2” to “+1” charge states, and e→c is the ZPL emission process. The reorganization energy (λ) is also represented in the diagram. b) Transition schematic diagram of the L_1 , M_1 , and H_1 of D_I spectrum in 4H-SiC. The 57 meV exciton binding energy in b) is cited from Ref. [15].

to the lowest energy L_1 state at low temperature, while the excitons created in the L_1 state will thermally excited to higher energy M_1 and H_1 states at a higher temperature. The L_1 line calculated by our first principles is $3.25 - 0.057 - 0.31 = 2.883$ eV, which is very close to the experimental value (2.902 eV). It is easy to inspire us that the “+1/+2” of Si_C defect center may correspond to the famous D_I center in the experiment. Next, we further demonstrate this conjecture from the first-principles calculation of the nonradiative capture cross-section.

3.3. Nonradiative Carrier Recombination

As a deep capture, the semi-occupied “+1” charge state of Si_C defect can capture a hole from the valence band and change to the “+2” charge state. The nonradiative capture rates can be expressed as^[30–32]

$$R_{ab} = \frac{1}{\hbar} \left(\frac{\pi}{\lambda kT} \right)^{1/2} \left[kT \sum_i \frac{|\sum_j \langle a | \partial H / \partial R_j | b \rangle V_j(i) / \sqrt{m_j}|^2}{w_j^2} \right] e^{-(\Delta E - \lambda)^2 / 4\lambda kT} \quad (2)$$

where a, b are the initial and final electronic states. H is the Hamiltonian of the system. $V_j(i)$ is the normalized phonon mode l vector with atom index i . w_j is the phonon frequency. R_i is the atomic configuration. m_j is the nuclear mass. ΔE is the transition energy. λ is the reorganization energy (the atomic relaxation energy after the electron state transition). In the present work, the transition energy and the reorganization energy of “+1/+2” of Si_C^h defect are 0.31 and 0.16 eV, respectively.

3.3.1. Defect Wave Function and Phonon Density of States

It can be seen from Equation (2) that the relevant electron–phonon coupling should be between the defect states and the VBM state. The defect state wave function is illustrated in **Figure 4** in a 200-atom supercell, and it can be seen that the wave function is mainly localized around the antisite Si atom.

The nonradiative capture rate calculation is phonon-dependent, and we need to calculate the phonon mode $V_l(i)$ and its frequency ω_l . We can diagonalize the following dynamic matrix to get the phonon spectrum.

$$M(i_1, i_2) = \frac{1}{(M_{i_1} M_{i_2})^{1/2}} \frac{\partial^2 E}{\partial i_1 \partial i_2} \quad (3)$$

The l th eigenvector of M will be $M_{i_1}^{1/2} V_l(i)$, and the eigenvalue will be $(\hbar \omega_l)^2$. Note $\partial^2 E / \partial i_1 \partial i_2 = \partial F_{i_1}(i_2) / \partial i_2$, thus we can numerically displace atoms i_2 , while using the Hellman–Feynman theory to calculate the atomic force $F_{i_1}(i_2)$ for all the atoms i_1 . However, the phonon modes calculation of our defective supercell requires 200×3 self-consistent calculations, which is very expensive. The “combined dynamic matrix” (CDM) method was proposed in our previous work, when both i_1 and i_2 are away from the defect center (beyond a cutoff distance R_c), the $\partial^2 E / \partial i_1 \partial i_2$ can be approximated by $\partial^2 E_{\text{bulk}} / \partial i_1 \partial i_2$.^[30] For the atoms within an R_c radius surrounding the defect center, we need numerical displacements to calculate their $\partial^2 E / \partial i_1 \partial i_2$. It is found that when the cutoff radius is 3.18 Å, the phonon spectrum obtained by the CDM method is in good agreement with the result calculated by using all of the atom explicit displacement.^[30] In this article, the CDM method is adopted, and the cutoff radius is set to 3.2 Å. The calculated phonon density of states is shown in **Figure 5a–d**, and we can see some localized phonon peaks lying in the gap between the acoustic and optic branches. In the neutral charge state, the Si_C^h defect has almost tetrahedral symmetry, and the associated triplet modes can split into a singlet 80.0 meV (A_1 symmetry) and a doublet 81.3 meV

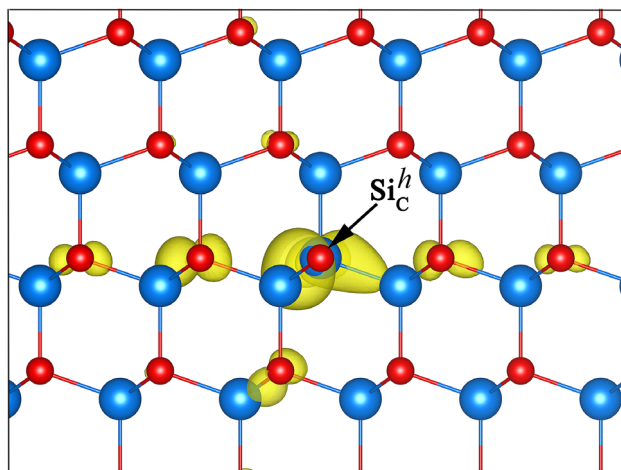


Figure 4. The square of wavefunctions of defect levels of Si_C^h defect in the 200-atom supercell calculated using the HSE density functional theory (DFT) function.

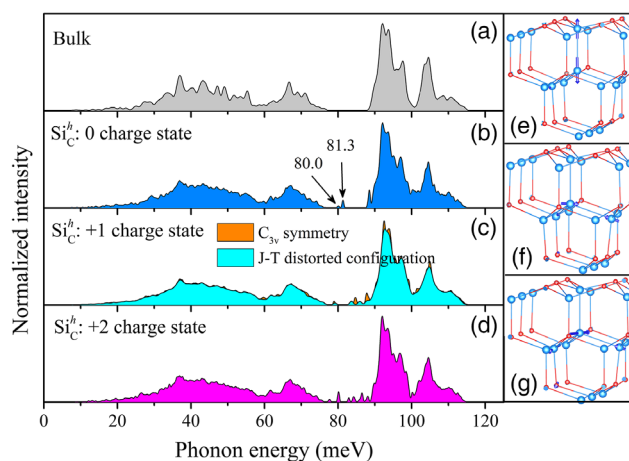


Figure 5. The phonon densities of: a) 4H-SiC bulk and Si_C^h defect at: b) “0”, c) “+1”, and d) “+2” charge states in the 200-atom supercell. The vibration schematic diagrams of: e) singlet 80.0 meV and f,g) doublet 81.3 meV phonon modes of “0” charge state defect. In c), orange and cyan data indicate the phonon densities of C_{3v} symmetry and Jahn–Teller distorted configurations of “+1” charge state defect.

(E symmetry). **Figure 5e–g** shows the vibration schematic diagrams of the localized phonon modes, from which we can see that the localized phonon modes in the gap are all related to the Si antisite and its nearby Si atoms. Sadowski and coworkers have proved that the gap phonon modes associated with the D_I center are derived from the vibration of the Si atom as their frequencies hardly shift in ^{13}C enriched material,^[33] which is consistent with our results.

3.3.2. Jahn–Teller Effect Analysis

It should be noted that the “+1” charge state of the antisite defect Si_C^h is a hole center with an incompletely filled degenerate ground state. Therefore, it should be subject to Jahn–Teller coupling. While the electrons in the “+2” charge state prefer parallel spins, and the high-spin ground state is not subject to a Jahn–Teller distortion. As shown in **Table 2**, after Jahn–Teller distortion, the symmetry of the “+1” charge state defect changes from C_{3v} to C_{1h} . The length of the Si–Si bond parallel to the c axis in the C_{3v} symmetry defect is 2.166 Å, and the lengths of the other three Si–Si bonds are 2.179 Å. The distorted configuration presents one larger Si–Si bond (by $\approx 2.1\%$) and two shorter bonds ($\approx 0.7\%$) compared with the bond length (2.179 Å) of the undistorted geometry, while the distance of the Si–Si bond parallel to

Table 2. Structural parameters and total energies for “+1” charge state antisite defect Si_C^h in 4H-SiC for the symmetric C_{3v} and most stable Jahn–Teller distorted configurations.

Defect	Point group	$d_{\text{Si-Si}} (\text{ to } c) [\text{\AA}]$	$d_{\text{Si-Si}} [\text{\AA}]$	Total energy [eV]
Si_C^{+1}	C_{3v}	2.166	2.179	−1744.623
Si_C^{+1} (J–T effect)	C_{1h}	2.167	2.163, 2.164, 2.224	−1744.693

the c axis is almost unchanged. The distorted configuration is more stable, with a total energy of 70 meV lower than that with C_{3v} symmetry. The neutral and “+2” charge states defects are not subject to Jahn–Teller distortion, which will affect our aforementioned calculation results of the transition levels and ZPL, but the effect is almost negligible. In addition, the Jahn–Teller effect will also influence the vibration frequency. As shown in Figure 5c, the distorted configuration only makes phonon models in the gap shift slightly. The defect-related phonon modes in the bandgap are almost negligible compared with the overall phonon modes of the system, which should not affect the following nonradiative recombination results. Therefore, the Jahn–Teller effect has not been considered in the following calculation in this article.

The Jahn–Teller effect often causes the splitting of bands in the photoluminescence excitation (PLE) spectrum, but it has not been reported in the experimental work of 4H-SiC. Egilsson and Storasta presented the PLE spectra at 2 K of the D_I in 4H-SiC, and a series of lines (named 2S, 3S, and 4S) are observed between 45 and 62 meV above the L_1 line in their PLE spectra.^[10,15] The authors proposed that the final states of the transitions corresponding to these lines were interpreted as effective-mass-like, excited electron states. We found that the energy difference between the main peaks of 2S and 3S (≈ 9 meV) is very close to the energy difference between L_1 and M_1 (≈ 8 meV), and the energy difference between the main peaks of 3S and 4S (≈ 4 meV) is very close to the energy difference between M_1 and H_1 (≈ 3 meV). In our calculation, the antisite defect-related degenerate E orbit will split under the combined effect of Jahn–Teller distortion and spin–orbit coupling, and the splitting is about 50 meV. The energy difference between the main peak of 2S and L_1 (≈ 47 meV) in their experiment is very close to the calculated splitting energy of the degenerate E states, thus we hypothesized that the absorption peaks of 2S, 3S, and 4S in the experimental PLE spectrum may originate from the transition from the split ground state of antisite defect Si_C to the excited states of L_1 , M_1 , and H_1 . Therefore, it is further suggested that the antisite defect Si_C with the Jahn–Teller effect in the “+1” charge state may be the source of the D_I center in 4H-SiC.

3.3.3. Calculated Capture Cross-Sections

According to Equation (2), we can obtain the transition rate R_{ab} for the VBM state to the defect state. In a defective supercell, the transition rate R_{ab} is often written as $C_{\text{non-rad}} \times N_d$,^[34] where $C_{\text{non-rad}}$ is a capture rate constant and N_d is the defect density. In our model, $N_d = 1/V$ (V is the volume of the supercell). Hence $C_{\text{non-rad}} = R_{ab} \cdot V$. Further, we can obtain the hole capture cross-section by $\sigma_{ab} = C_{\text{non-rad}}/\nu_p$, here ν_p is the mean hole thermal velocity $\nu_p = \sqrt{3k_B T/m_p}$. k_B is Boltzmann’s constant, T is the temperature, and m_p is the effective mass of the hole. In 4H-SiC, the effective masses of the hole in the basal plane and parallel to the c axis are about $0.66m_0$ and $1.75m_0$, respectively.^[35] Here m_0 is the mass of the free electron. In the present work, the hole effective masses of $0.66m_0$ and $1.75m_0$ were used to calculate the capture cross-sections, respectively, and the average values of the two results are shown in Figure 6a. At 150 K, the calculated capture cross-section for $\Delta E = 0.31$ eV is $2.5 \times 10^{-13} \text{ cm}^2$, which is about an order of magnitude larger than the experimental result ($2.0 \times 10^{-14} \text{ cm}^2$).^[7] Christenson et. al proposed that different correction methods may lead to an error of about 0.1 eV in the defect transition energy level calculations.^[36] Therefore, the transition energy level of 0.35 eV in the experimental D_I center was used to calculate the capture cross-section. The obtained result was $4.8 \times 10^{-14} \text{ cm}^2$, which was slightly larger than the experimental value. This may be because the Coulomb repulsion between the positively charged defect center and the hole is not considered in our work, so our calculation results are somewhat overestimated. One might suspect that the electrons in the conduction band might fall into the semi-occupied “+1” charge state of antisite defect Si_C, emitting the zero-phonon line (ZPL) of 2.70 eV ($E_{\text{Gap}} - 0.55$) ($c \rightarrow a$ process in Figure 2), while this would not be observed experimentally. In practice, whether the “+1” charge state continues to nonradiatively capture a hole change to a “+2” charge state or radiatively capture an electron change to a “0” charge state depends on the transition probability of the two processes. Based on Fermi’s gold rule,^[37,38] we can obtain that the capture rate constant of an electron falls into the “+1” charge state of

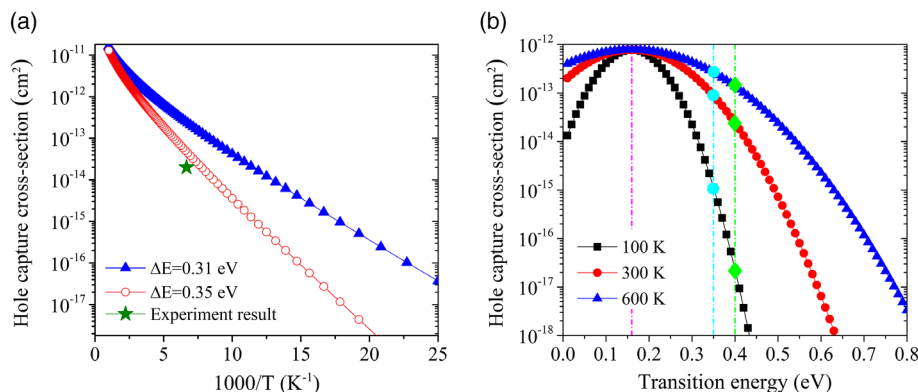


Figure 6. Calculated: a) temperature dependence and b) transition energy dependence of hole capture cross-section of Si_C^h defect in 4H-SiC. In (b), the colored diamonds represent the capture cross-sections of Si_C^h defect with transition energies of 0.35 eV and 0.40 eV, respectively.

antisite defect Si_C is $C_{\text{rad}} = 4.6 \times 10^{-17} \text{ cm}^3 \text{ s}^{-1}$, which is nine orders of magnitude smaller than the capture rate constant of a hole jump to “+1” charge state center ($C_{\text{non-rad}} = 7.6 \times 10^{-8} \text{ cm}^3 \text{ s}^{-1}$). In the p -type or semi-insulated samples, the hole concentration in the valence band is greater than or equal to the concentration of electrons in the conduction band, and the probability of the transition from “+1” to “+2” charge state is much greater than the probability of the transition from “+1” back to “0” charge state. For n -type samples, the electron concentration (n) in the conduction band is greater than the hole concentration (p) in the valence band under small injection. Thus, the transition probability of electrons from the conduction band to the “+1” defect center is $C_{\text{rad}} \times n$, while the transition probability of holes from the valence band to the “+1” defect center is $C_{\text{non-rad}} \times N_\text{d}$. N_d is the concentration of antisite defect Si_C , and the value in the irradiation sample after high-temperature annealing is almost above $1.0 \times 10^{12} \text{ cm}^{-3}$.^[7,10] It is easy to estimate that $C_{\text{rad}} \times n$ is close to $C_{\text{non-rad}} \times N_\text{d}$ when the intrinsic electron concentration in the sample is as high as 10^{21} cm^{-3} . Thus, we believe that the absence of luminescence related to the transition “0/+” of Si_C defect in the experiments is due to the low intrinsic electron concentration in the sample. Considering that the calculated transition energy level, ZPL, and capture cross-sections of Si_C^h defect are all in good agreement with the corresponding values of D_I center in the experiment, we propose that the transition between the “+1” and “+2” charge states of Si_C defect is responsible for the D_I center in 4H-SiC.

Godignon et al. reported 4H-SiC Schottky diodes with high- and low-temperature resistance, which can work stably at about $-170 \sim 300^\circ\text{C}$.^[39] Huang et al. proposed a concept to regulate the defect levels in semiconductors while maintaining the electronic properties of the host materials via specific alloying,^[40] and Sensoy et al. reported that strain effects can regulate the transition energy of defect in MoS_2 .^[41] Therefore, we have studied the transition energy dependence of the capture cross-section at 100, 300, and 600 K, and the results are shown in Figure 6b. Due to the term $e^{-(\Delta E - \lambda)^2 / 4\lambda kT}$ in Equation (2), when the transition energies are equal to the reorganization energy (0.16 eV), the hole capture cross-sections at all temperatures have the same maximum value, which is close to the order of 10^{-12} cm^2 . When the transition energy level is not equal to 0.16 eV, the hole capture cross-sections of Si_C^h defect will increase with T as about $e^{-(\Delta E - \lambda)^2 / 4\lambda kT}$. When the transition energy is fixed at 0.35 eV, the capture cross-section at 100 K is only $1.1 \times 10^{-15} \text{ cm}^2$. When the temperature rises from 100 to 300 K, the capture cross-section increases almost by two orders of magnitude, reaching $8.9 \times 10^{-14} \text{ cm}^2$. With the continuous temperature increase, the rise of the capture cross-section shows a slowing trend. At 600 K, the capture cross-section is $2.6 \times 10^{-13} \text{ cm}^2$, which is only about three times that at 300 K. As can be seen from the Figure 6b, with the increase of defect transition energy levels, the hole capture cross-sections at different temperatures will decrease a certain extent. When the defect transition energy level increases from 0.35 to 0.40 eV, the capture cross-sections at 600 and 300 K will decrease to 53.8% and 27.0%, while the capture cross-section at 100 K can be reduced by two orders of magnitude. The working temperature of the 4H-SiC sample and the position of the defect transition

level are very sensitive to the carrier capture cross-section of the defect center.

4. Conclusion

In summary, this work provides an idea for accurately identifying specific point defects in semiconductors. Based on first-principles calculations, our calculated ZPL and hole capture cross-sections of Si_C^h defect are highly consistent with the D_I center-related results in the experiment. We proposed that the antisite defect Si_C may be the origin of the D_I defect center in 4H-SiC. Our approach is not just unique to the SiC system, and it can be readily applied to other 3D or 2D semiconductor materials. In addition, the carrier capture capacity of the defect centers in the samples can be designed according to the actual demand by modifying the defects' transition energy levels, and the optimal design of the point defects of semiconductor materials in different applications can be realized.

Acknowledgements

This work was financially supported by the National Natural Science Foundation of China (Grant No. 12004204, 12274360, 11964022), the Natural Science Foundation of Inner Mongolia Autonomous Region (Grant No. 2020BS01003), and the Key Research Program of the Frontier Science of the Chinese Academy of Sciences (Grant No. QYZDB-SSW-SLH042).

Conflict of Interest

The authors declare no conflict of interest.

Data Availability Statement

The data that support the findings of this study are available from the corresponding author upon reasonable request.

Keywords

4H-SiC, capture cross-section, D_I center, nonradiative recombination

Received: July 4, 2022

Revised: September 9, 2022

Published online: October 13, 2022

- [1] D. Nakamura, I. Gunjishima, S. Yamaguchi, T. Ito, A. Okamoto, H. Kondo, S. Onda, K. Takatori, *Nature* **2004**, 430, 1009.
- [2] F. F. Wang, Z. Zhang, *CPSS Trans. Power Electron. Appl.* **2016**, 1, 13.
- [3] T. Kimoto, *Jpn. J. Appl. Phys.* **2015**, 54, 040103.
- [4] C. G. Hemmingsson, N. T. Son, A. Ellison, J. Zhang, E. Janzén, *Phys. Rev. B* **1998**, 58, R10119.
- [5] Y. Negoro, T. Kimoto, H. Matsunami, *Appl. Phys. Lett.* **2004**, 85, 1716.
- [6] S. Castelletto, B. C. Johnson, V. Ivády, N. Stavrias, T. Umeda, A. Gali, T. Ohshima, *Nature Mater.* **2014**, 13, 151.
- [7] J. Zhang, L. Storasta, J. P. Bergman, N. T. Son, E. Janzén, *J. Appl. Phys.* **2003**, 93, 4708.

- [8] C. Haberstroh, R. Helbig, R. A. Stein, *J. Appl. Phys.* **1994**, 76, 509.
- [9] T. A. Kennedy, J. A. Freitas, S. G. Bishop, *J. Appl. Phys.* **1990**, 68, 6170.
- [10] L. Storasta, F. H. C. Carlsson, S. G. Sridhara, J. P. Bergman, A. Henry, T. Egilsson, A. Hallén, E. Janzén, *Appl. Phys. Lett.* **2000**, 78, 46.
- [11] L. Patrick, W. J. Choyke, *Phys. Rev. B* **1972**, 5, 3253.
- [12] A. Fissel, W. Richter, J. Furthmüller, F. Bechstedt, *Appl. Phys. Lett.* **2001**, 78, 2512.
- [13] A. Gali, P. Deák, E. Rauls, N. T. Son, I. G. Ivanov, F. H. C. Carlsson, E. Janzén, W. J. Choyke, *Phys. Rev. B* **2003**, 67, 155203.
- [14] T. A. G. Eberlein, R. Jones, S. Öberg, P. R. Briddon, *Phys. Rev. B* **2006**, 74, 144106.
- [15] T. Egilsson, J. P. Bergman, I. G. Ivanov, A. Henry, E. Janzén, *Phys. Rev. B* **1999**, 59, 1956.
- [16] S. I. Maximenko, J. A. Freitas, N. Y. Garces, E. R. Glaser, M. A. Fanton, *J. Electron. Mater.* **2008**, 38, 551.
- [17] Y. Gu, L. Shi, J.-W. Luo, S.-S. Li, L.-W. Wang, *Phys. Status Solidi RRL* **2022**, 16, 2100458.
- [18] B. Magnusson, N. T. Son, A. Csóré, A. Gällström, T. Ohshima, A. Gali, I. G. Ivanov, *Phys. Rev. B* **2018**, 98, 195202.
- [19] M. Posselt, F. Gao, W. J. Weber, *Phys. Rev. B* **2006**, 73, 125206.
- [20] W. Jia, J. Fu, Z. Cao, W. Long, X. Chi, W. Gao, L. W. Wang, *J. Comput. Phys.* **2013**, 251, 102.
- [21] W. Jia, Z. Cao, L. Wang, J. Fu, X. Chi, W. Gao, L.-W. Wang, *Comput. Phys. Commun.* **2013**, 184, 9.
- [22] P. E. Blöchl, *Phys. Rev. B* **1994**, 50, 17953.
- [23] J. P. Perdew, K. Burke, M. Ernzerhof, *Phys. Rev. Lett.* **1996**, 77, 3865.
- [24] D. R. Hamann, *Phys. Rev. B* **2013**, 88, 085117.
- [25] J. Heyd, G. E. Scuseria, M. Ernzerhof, *J. Chem. Phys.* **2003**, 118, 8207.
- [26] J. Heyd, G. E. Scuseria, M. Ernzerhof, *J. Chem. Phys.* **2006**, 124, 219906.
- [27] M. Stockmeier, R. Müller, S. A. Sakwe, P. J. Wellmann, A. Magerl, *J. Appl. Phys.* **2009**, 105, 033511.
- [28] S. H. Wei, *Comp. Mater. Sci.* **2004**, 30, 337.
- [29] T. A. G. Eberlein, C. J. Fall, R. Jones, P. R. Briddon, S. Öberg, *Phys. Rev. B* **2002**, 65, 184108.
- [30] L. Shi, L.-W. Wang, *Phys. Rev. Lett.* **2012**, 109, 245501.
- [31] L. Shi, K. Xu, L.-W. Wang, *Phys. Rev. B* **2015**, 91, 205315.
- [32] L. Shi, K. Xu, L.-W. Wang, *Phys. Rev. B* **2018**, 97.
- [33] H. Sadowski, N. Schulze, T. Frank, G. Pensl, M. Laube, R. Helbig, *Mater. Sci. Forum* **2001**, 353–356, 401.
- [34] J. Nelson, in *The Physics Of Solar Cells*, Imperial College, London **2003**.
- [35] N. T. Son, P. N. Hai, W. M. Chen, C. Hallin, B. Monemar, E. Janzén, *Phys. Rev. B* **2000**, 61, R10544.
- [36] S. G. Christenson, W. Xie, Y. Y. Sun, S. B. Zhang, *J. Appl. Phys.* **2015**, 118, 135708.
- [37] A. F. van Driel, G. Allan, C. Delerue, P. Lodahl, W. L. Vos, D. Vanmaekelbergh, *Phys. Rev. Lett.* **2005**, 95, 236804.
- [38] H. S. Zhang, L. Shi, X. B. Yang, Y. J. Zhao, K. Xu, L. W. Wang, *Adv. Opt. Mater.* **2017**, 5, 1700404.
- [39] P. Godignon, X. Jorda, M. Vellvehi, X. Perpina, V. Banu, D. Lopez, J. Barbero, P. Brosselard, S. Massetti, *IEEE Trans. Ind. Electron.* **2011**, 58, 2582.
- [40] B. Huang, M. Yoon, B. G. Sumpter, S.-H. Wei, F. Liu, *Phys. Rev. Lett.* **2015**, 115, 126806.
- [41] M. G. Sensoy, D. Vinichenko, W. Chen, C. M. Friend, E. Kaxiras, *Phys. Rev. B* **2017**, 95, 014106.